A new method to retrieve relative humidity profiles from a synergy of Raman lidar, microwave radiometer and satellite

Chengli Ji[1], Qiankai Jin[2], Feilong Li[2], Yuyang Liu[2], Zhicheng Wang[1], Jiajia Mao[1], Xiaoyu Ren[1], Yan Xiang[4], Wanlin Jian[5,6], Zhenyi Chen*[2,3] and Peitao Zhao*[1]

[1] CMA Meteorological Observation Centre, Beijing, 100081, China

[2] State Environmental Protection Key Laboratory of Food Chain Pollution Control, Beijing Technology and Business University, Beijing, 100048, China

[3] Key Lab. of Environmental Optics & Technology, Anhui Institute of Optics and Fine Mechanics, Chinese Academy of Sciences, Hefei, 230031, China

[4] Institutes of Physical Science and Information Technology, Anhui University, Hefei, 230031, China

[5] Sichuan Meteorological Observation and Data Center, Chengdu, 610072, China

[6] Sichuan Meteorological Observatory Heavy rain and Drought‑Floor Disaster in Plateau and Basin Key Laboratory of Sichuan Province, Chengdu, 610072, China

*Corresponding author: E‑mail: zychen@btbu.edu.cn (Zhenyi Chen),

peitaozhao@163.com (Peitao Zhao)

Abstract Precise continuous measurements of relative humidity (RH) vertical profiles in the troposphere have emerged as a considerable scientific issue. In recent years, a combination of diverse ground-based remote sensing devices has effectively facilitated RH vertical profiling, leading to enhancements in spatial resolution and, in certain instances, measurement accuracy. This work introduces a newly developed approach for obtaining continuous RH profiles by integrating data from a Raman lidar, a microwave radiometer, and satellite sources. RH profiles obtained using synergistic approaches are subsequently compared with radiosonde data throughout a five-month observational study in China. Our suggested method for RH profiling demonstrates optimal concordance with the best correction coefficients R of 0.94 in Huhehaote

32 (HHHT), 0.92 in Yibin (YB) and 0.93 in Qingyuan (QY), respectively. Accordingly, the mean

33 bias (MB) reached the lowest values of 4.93% in HHHT, 2.63% in YB and 2.40% in QY. The

34 mean value of RH decreased with height and presented seasonal characteristics in QY. Finally,

35 the RH height-time evolution in a convective case was analyzed. This study firstly integrates

36 satellite data into ground-based measurement to provide information on RH profiles in China,

37 which may aid in further evaluating their regional characteristic and their impacts on the local

38 ecosystem.

40 **Keywords:** relative humidity profiles, Raman lidar, microwave radiometer, satellite

1. Introduction

43 Relative humidity (RH) is a crucial parameter in characterizing aerosol-cloud interactions (Fan

44 et al., 2007) and is necessary as input for weather forecasting models (Petters and Kreidenweis,

45 2007; Wex et al., 2008; Mochida, 2014). The combination of these RH profiles with aerosol

46 optical data allows us to obtain hygroscopic growth factors for different aerosol types (Zieger

47 et al., 2013; Granados et al., 2015). However, the temporal resolution of routine observations

48 performed by weather services is rather low, typically with one or two radiosonde launches per

49 day (Schmetz et al., 2021). And significant mesoscale weather phenomena, including the

50 movement of frontal systems and the formation of convective boundary hygroscopic growth or

51 clouds, transpire rapidly, making it more challenging to adequately monitor the evolution of

52 atmospheric profiles (Kang et al., 2019; Long et al., 2023; Chen et al., 2024). Consequently,

53 precise information with great temporal resolution is essential for examining these events.

54 The current Raman lidar technology enables concurrent measurements of temperature and

55 water vapor mixing ratio profiles to derive RH profiles (Reichardt et al., 2012; Brocard et al.,

56 2013). But it requires calibration by the use of collocated and simultaneous observations from

57 a radiosonde or microwave radiometer (MWR) (Mattis et al., 2002; Madonna et al., 2011; Foth

58 et al., 2015). In addition, the average error of Raman lidar is relatively small within the

59 effective height range but limited in the higher height detection.

60 MWR is another way to provide atmospheric RH observations with high temporal resolution

61 (Hogg et al., 1983; Ware et al., 2003; Zhang et al., 2024). Although MWR has a certain

62 penetration ability for harsh weather conditions such as clouds, their vertical resolution and

63 accuracy are not high, especially for RH which vary greatly (Xu et al., 2015). Thus, it is

64 challenging to deliver continuous high-resolution RH information with a single instrument.

65 The synergy of complementary information from both active and passive instruments can

66 provide a more comprehensive understanding of atmospheric processes (Stankov, 1995;

删除: Our suggested method for RH profiling demonstrates optimal concordance with the best correction coefficients R of 0.94 in Huhehaote (HHHT), 0.92 in Yibin (YB) and 0.93 in Qingyuan (QY), respectively.

删除: z

删除: MVR

删除: MVR

删除: For accurate RH profile retrieval at higher heights, space-borne MVR have global detection capabilities and are highly effective for oceanic skies and remote land areas (Zhang et al., 2022; Wang et al., 2023). But the time resolution of polar orbit satellites equipped with MVR is determined by the repeated coverage time of the satellite orbit (Skou, et al., 2022). A single satellite can generally only achieve repeated observations twice a day, and the time resolution is also relatively low.

删除:
As previously indicated,

67 Furumoto et al., 2003; Delanoë and Hogan, 2008; Blumberg et al., 2015; Tuner et al., 2021).

68 For example, when both Raman lidar and MWR are measuring collocated and simultaneously,

69 continuous temperature, water vapor profiles and thus RH profiles can be obtained

70 operationally (Navas-Guzmán et al., 2014; Barrera-Verdejo et al., 2016; Foth et al., 2017;

71 Toporov et al., 2020). However, most of their algorithms primarily utilize statistical methods,

72 performing data fusion between different instruments based on long-term time-series data from

73 individual locations. While these approaches are suitable for observations at single stations,

74 they lack universality when applied to scenarios requiring data integration from multiple sites

75 or broader geographical coverage. Moreover, replacing instruments or equipment may also

76 introduce additional inconsistencies.

77 For accurate RH profile retrieval at higher heights, satellites have global detection capabilities

78 and are highly effective for oceanic skies and remote land areas (Zhang et al., 2022; Wang et

79 al., 2023). For example, Wang et al. measured the subgrid-scale variability of critical relative

80 humidity (RH_c) to investigate the cloud parameterization based on the diagnostics from

81 CloudSat/CALIPSO satellite data. Some deal with the retrieval of the atmospheric layer

82 averaged relative humidity profiles using data from the Microwave Humidity Sounder (MHS)

83 onboard the MetOp satellite (Gangwar et al., 2014). Geostationary Operational Environmental

84 Satellite (GOES)-13 and the Moderate-Resolution Imaging Spectroradiometer (MODIS) data

85 are also be combined to estimate hourly relative humidity at the surface level (Ramírez-

86 Beltrán et al., 2019). Another sounder, SAPHIR, onboard MEGHA-TROPIQUES provides

87 measurements in six water vapour channels for sounding the atmospheric humidity. Brogniez

88 et al. (2013) and Gohil et al. (2013) have shown the potential of SAPHIR sounder in retrieving

89 the atmospheric humidity profile.

90 But the time resolution of polar orbit satellites is determined by the repeated coverage time of

91 the satellite orbit (Skou, et al., 2022). A single satellite can generally only achieve repeated

92 observations twice a day, and the time resolution is also relatively low. Furthmore, few

93 observations are available from China's satellite Fenyun (FY), to the use of synthetic retrieval

94 of RH information. This study aims to introduce a novel technique that integrates Raman lidar,

95 MWR, and satellite data (FY4B) using an optimum estimating methodology. It is given with a

96 focus on two aspects: i) Evaluation of the proposed synergetic method, and ii), investigation of

97 the RH characteristics at different heights and in different geographic regions. This paper is

98 thus structured as follows. Descriptions of the individual equipment is presented in Section 2.

99 Section 3 illustrates the process of the new synergetic algorithm combining the ground-based

删除: Furthermore, at the time of the study,

100 and satellite data. Section 4 presents the RH statistic results and its time-height evolution in a
101 strong convective case. Finally, conclusions are summarized in Section 5.

102 **2. Instrumentation**

103 *2.1 Raman lidar*

104 The Raman lidar method can assess the water vapor mixing ratio profiles through inelastic
105 backscatterring signals from nitrogen at 387 nm and from water vapor at 407 nm (Whiteman,
106 1992; Mattis et al., 2002; Adam et al., 2010). At the lowest height, the intersection of the laser
107 beam with the receiver's field of view in the bistatic system is incomplete. Nevertheless, the
108 overlap of both Raman channels is presumed to be equivalent; thus, the overlap effect could be
109 minimal concerning water vapor measurements. The collected water vapor measurements, then
110 along with concurrent temperature profiles from a co-located MWR allow us to obtain RH
111 profiles. The vertical and temporal resolution of Raman lidar and other instruments are listed in
112 Table 1.

113 *2.2 Microwave Radiometer (MWR)*

114 The Microwave Radiometer (MWR) serves as a passive instrument designed to measure
115 atmospheric emissions across two frequency bands within the microwave spectrum (Cimini et
116 al., 2006; Crewell and Löhnert, 2007). There are seven channels set along the 22.235 GHz H_2O
117 absorption line. Humidity information can be extracted from these observations. The seven
118 channels of the alternative band from 51 to 58 GHz within the O_2 absorption complex
119 encompass the vertical temperature profile data. Consequently, the fully automatic MWR
120 enables the derivation of temperature and humidity profiles with a temporal resolution of up to
121 5 minutes. The method for inverting temperature and humidity profiles is the neural network
122 method in this study. It uses statistical methods to optimize the long-term average radiosonde
123 data and relies on previous radiosonde data (Yang et al., 2023).

124 *2.3 Radiosonde data*

125 We use radiosonde data from the China Meteorological Administration (CMA) station for
126 reference analysis. It is located in the same place as the Raman lidar, and provides on-site
127 measurements of atmospheric pressure, temperature, and RH. During the observing campaign,
128 radiosondes were launched twice a day (08:00 LST and 20:00 LST). The height of the
129 radiosonde balloon can be determined by the ascent time of the radiosonde balloon. The
130 vertical resolution of the raw data is 3 m/layer. To match other data, the vertical resolution of
131 the raw data is interpolated to 30 m (0-3000 m) and 250 m (3000-10000 m), respectively.

132 *2.3 Satellite*

删除: But the signal-to-noise ratio (SNR) decreases with height, thus the threshold of SNR should be set. Here we set the Raman SNR threshold value of 3. The Raman signal starts with the first SNR greater than 3 and ends with five consecutive SNRs less than 3.

删除: MVR

删除:

删除: *V*

删除: V

删除: V

删除: The uncertainty of the instrument can reach a confidence level of 95.5%.

133 In 2016 and 2021, China successfully deployed two second-generation geostationary
134 meteorological satellites, Fengyun-4A (FY4A) and Fengyun-4B (FY4B), both equipped with
135 the Geostationary Interferometric Infrared Sounder (GIIRS). The GIIRS therefore became the
136 first geostationary orbiting meteorological satellite (Yang et al., 2023). This approach could
137 achieve the detection of weather systems across China and its neighboring regions with high
138 temporal and spatial resolution. So it enables a more comprehensive understanding of the
139 atmospheric vertical structure, including the retrieval of atmospheric temperature profiles for
140 1000 m layers and moisture profiles for 2000 m layers (Yang et al., 2017), respectively. In
141 comparison to FY4A, the GIIRS on FY4B exhibits a broader spectral range, improved spectral
142 resolution in the long-wave IR band, and superior radiometric calibration accuracy and
143 detection sensitivity (Sufeng et al., 2022). Specifically, the temporal resolution of GIIRS has
144 enhanced from 2.5 hours for FY4A to 2 hours for FY4B, and the spatial resolution has
145 progressed from 16000 m to 12000 m at nadir. The atmospheric humidity profiles utilized in
146 this study, derived from GIIRS, are generated through the neural network algorithm created by
147 the National Satellite Meteorological Centre (NSMC) (Bai et al., 2022). The data is available
148 online: http://fy4.nsmc.org.cn/nsmc/en/ theme/FY4B.html (accessed on 12 December 2024).

3. Methods and evaluation

3.1 Lidar, MWR and satellite synergetic algorithm

This study aims to obtain a continuous time series of RH profiles by integrating ground-based
remote sensing techniques, including Raman lidar, MWR, and satellite data, in a
straightforward manner to facilitate a wide range of applications. The retrieval process
involves a systematic four-step algorithm that integrates the Raman lidar water mixing ratio
profile and MWR brightness temperatures along with satellite data. The retrieval framework is
shown as in Fig. 1 and the retrieval process is detailed in the following paragraphs.

Step 1: Data quality control. Data with quality control codes of 0 and 1 for FY4B and 0 for
ground-based remote sensing data is selected. The lidar only retains data with a SNR value
greater than 3. The threshold value of the SNR is set as 3 based on our extensive comparisons
with radiosonde data from CMA's long-term observations. The results indicate that selecting
lidar signals with signal-to-noise ratios (SNR) >3 can significantly improve the consistency
between retrieved RH profiles and radiosonde measurements. So in the data selection period,
the Raman signal starts with the first SNR greater than 3 and ends with five consecutive SNRs
less than 3. The real-time observing data are designated as R_{radio}, R_{lidar}, R_{MWR} and $R_{satellite}$ in Fig.
2.

删除: MVR

删除: V

删除: MVR

Step 2: Data spatial-temporal matching. This process aims to match the above quality-controlled data with the radiosonde data at a height of 0-10000 m in time and space before the synergetic algorithm. For the time matching, temperature from MWR and water vapor data from Raman lidar are selected corresponding to the radiosonde data time (00:80 LST and 20:00 LST). In terms of spatial matching, the FY4B data is selected from the nearest grid point to the ground observing station for the horizontal scale. The data at vertical heights are interpolated to the resolution of 30 m (0-3000 m) and 250 m (3000-10000 m).

Step 3: Correction coefficient determination. The deviation between the temperature and humidity data of satellites and ground-based remote sensing data at each height is quantitatively calculated and analyzed to prepare for the optimal stitching process in the next step. Here the deviation of lidar, MWR and FY4B is designated as D_{lidar}, D_{MWR} and $D_{satellite}$, respectively.

$$D_{lidar}=R_{lidar}-R_{radio} \tag{1}$$

$$D_{MWR}=R_{MWR}-R_{radio} \tag{2}$$

$$D_{satellite}=R_{satellite}-R_{radio} \tag{3}$$

The correction coefficients C_{lidar}, C_{MWR} and $C_{satellite}$ are calculated as follows

$$C_{Lidar}=(|D_{satellite}|+|D_{MWR}|)/[2*(|D_{satellite}|+|D_{MWR}|+|D_{lidar}|)] \tag{4}$$

$$C_{MWR}=(|D_{satellite}|+|D_{lidar}|)/[2*(|D_{satellite}|+(|D_{MWR}|+|D_{lidar}|)] \tag{5}$$

$$C_{satellite}=(D_{MWR}+D_{MWR})/[2*-(|D_{satellite}|+|D_{MWR}|+|D_{lidar}|)] \tag{6}$$

Step 4: Synergetic algorithm iteration and evaluation: Based on the above spatial-temporal data matching and correction coefficients calculation at different heights, a dynamic optimal stitching algorithm (Fig. 2) is conducted. To ensure the independence between the tested sample and the true value, the temperature and humidity profiles of the current time are fused using the correction coefficient of the previous time, and then compared with the radiosonde data at the same time for evaluation. The correlation coefficient (R), the root mean square error (RMSE), and mean bias (MB) are used as inspection indexes. Finally, the retrieved RH information S_{RH} could be obtained through the following formula.

$$S_{RH}=R_{satellite}*C_{satellite}+ R_{MWR}*C_{MWR}+R_{lidar}*C_{Lidar} \tag{7}$$

From the process we can see that compared to these existing techniques, our new method not only incorporates satellite data but also dynamically determines optimal fusion coefficients. Because the fusion coefficients are dynamically determined by comparing the deviations from

删除: MVR

删除: each instrument

删除: MVR

删除: The calculation of correction coefficients C_{lidar}, C_{MVR} and $C_{satellite}$ are also presented in Fig. 2.

other measurements with the reference of radiosonde, it highlights that this new algorithm is real-time calibrated. And it can guarantee the device model independence and geographical adaptability. Thus it eliminates constraints imposed by equipment specifications or observation locations, ensuring broad applicability across diverse scenarios.

3.2 Error analysis

To evaluate the performance of the synergetic algorithm for RH profiles, a comparative analysis was conducted between retrieved values and actual radiosonde measurements. Let N represent the total number of samples. The measured value is designated as O_i, with i representing the sample label. The value obtained through the new synergetic algorithm is designated as G_i. The evaluation indicators consist of MB, mean absolute bias (MAB) and RMSE are defined by the following formulas:

$$MB = \frac{\sum_{i=1}^{N}(G_i - O_i)}{N} \tag{8}$$

$$MAB = \frac{\sum_{i=1}^{N}|G_i - O_i|}{N} \tag{9}$$

$$RMSE = \sqrt{\frac{\sum_{i=1}^{N}(G_i - O_i)^2}{N}} \tag{10}$$

4. Results

4.1 General statistic information

A five-month data set has been chosen for a statistical analysis of RH profiles. The observation period spans from July 1 to November 30, 2024. The observing elements are RH data from 47 stations in China (yellow circles in Fig. 3) at the height of 0-10000 m. To investigate RH retrieval accuracy, we provide the comparison results of four methods (lidar, MWR, satellite, and synergetic algorithm) utilizing the radiosonde data as the reference at 47 sites in Table 2. Then Huhehaote (HHHT, northern China), Yibin (YB, middle China) and Qingyuan (QY, southern China) are selected as 3 representative sites (red stars in Fig. 3) for more detailed analysis, as shown in Fig. 4 and Table 3.

Generally, the synergetic algorithm at 47 sites presents the maximum correlation coefficient R value of 0.98 with the minimum RMSE of 5.27% in Table 2. For three representative sites, the regression line from the synergetic algorithm at all heights similarly provides the best fitting results, with the largest correlation coefficients R of 0.94, 0.92 and 0.93 in HHHT, YB and QY respectively (Table 3). The correlation coefficient R for lidar measurement follows with

227 marginally higher values of 0.83 in HHHT, 0.86 in YB and 0.86 in QY, indicating its greater
228 applicability compared to other single instruments. MWR presents the lowest R of 0.74 and
229 0.80 in HHHT and YB, while performing better (R = 0.75) than that from satellite (R = 0.66) in
230 QY. In terms of RMSE, the lidar-, MWR- and satellite-derived RH all show values larger than
231 18% at three sites. The synergistic use of a multi-source algorithm decreases the RMSE down
232 to the lowest value of 10% in HHHT.

233 The regression line for lidar and MWR in HHHT, as illustrated in Fig. 4, exhibits a slope that is
234 less than that of the one-to-one line. This implies that greater variations arise with increased
235 RH in HHHT. Though the synergetic algorithm also presents similar trends, its RMSE
236 decreased to 26% in HHHT. The regression line of MWR and lidar in YB and QY are larger
237 than the one-to-one line, indicating the larger bias for less humid.

238 As RH vertical profiles are height-dependent, Fig. 5 presents the MB profiles observed at
239 different heights in terms of four methods. Generally, the MB in the RH of lidar in the lower
240 troposphere (below 3000 m) outperforms the other two single methods (MWR and satellite) at
241 three sites. No significant biases between radiosonde and lidar are noticeable. Specifically, the
242 lowest MB values (4.93% in HHHT, 2.63% in YB and 2.40% in QY) in the comprehensive
243 region of the tropospheric region are achieved when lidar data is incorporated into the
244 synergetic algorithm. This is because lidar is an active remote sensing technology with more
245 accuracy compared to MWR and satellite. The lidar data's efficacy is enhanced at heights
246 below 3000 m when integrated with data from other sources within the boundary layer.

247 However, the MB from lidar increased drastically above this height, up to the highest value
248 28.67% in HHHT, 29.91% in YB and 20.09 % in QY. It is reasonable that the atmosphere
249 changes so fast that radiosonde do not assess exactly the same air mass as lidar. In the
250 meantime, lidar is increasingly constrained at elevated heights because of a decreased SNR.
251 Hence lidar is more trustworthy in the lower layer, i.e. below 3000 m.

252 In contrast, the MB from satellite (FY4B) over 3000 m varied steadily within the range of
253 approximately 15% at three sites. Therefore the satellite data in the far height range would be
254 more reliable and could be employed in the synergetic algorithm at higher layers. Compared to
255 lidar and satellite, the MB from MWR gives the largest uncertainty in HHHT at all heights.
256 This may result from the discrepancy between the temperature recorded by the radiosonde and
257 that obtained from the MWR in HHHT. However, it yields relatively less variation than lidar
258 and satellite in YB and QY. Anyway, the synergetic method gives the best result for over three
259 observing sites at almost all heights. And accurate measurements of RH vertical profiles
260 provided here are highly beneficial for analyzing the hygroscopic growth of local aerosols.

删除: Generally, the synergetic algorithm at 47 sites presents the maximum correlation coefficient R value of 0.98 with the minimum RMSE of 5.27% in Table 2. For three representative sites, the regression line from the synergetic algorithm at all heights similarly provides the best fitting results, with the largest correlation coefficients R of 0.90, 0.91 and 0.93 in HHHT, YB and QY respectively (Table 3). The correlation coefficient R for lidar measurement follows with marginally lower values of 0.85 in HHHT, 0.85 in YB and 0.91 in QY, indicating its greater applicability compared to other single instruments. MVR presents the lowest R of 0.73 and 0.80 in HHHT and YB, while performing better (R = 0.84) than that from satellite (R = 0.78) in QY. In terms of RMSE, the lidar-, MVR- and satellite-derived RH all show values larger than 25% at three sites. The synergistic use of a multi-source algorithm decreases the RMSE down to the lowest value of 16% in QY.

删除: MVR

删除: MVR

删除: MVR

删除: MVR

删除: MVR

删除: MVR

261 The sources of the discrepancy can stem from several aspects. First, although all instruments
262 are co-located in the ground, radiosondes deviate at higher heights, and signals can be
263 disrupted if clouds are present. Second, satellites provide gridded data, requiring the selection
264 of ground observation points closest to its grid's latitude and longitude, which introduces
265 uncertainty. Finally, both MWR and satellite are passive remote sensing technologies, which
266 are inherently less precise than active remote sensing. Besides the inherent hardware difference,
267 the errors during the retrieval process (e.g., neural networks for MWR) are also unavoidable.

删除: MVR

删除: V

268 *4.2 Mean monthly analysis*

269 RH mean monthly vertical profiles have been derived from the synergistic method illustrated
270 in Fig. 6. Because RH profiles were retrieved from water ratio profiles and temperature profiles.
271 For this property, the RH seasonal behavior may be more complicated. For example, no
272 obvious seasonal behavior of RH profiles is found in HHHT or YB. However, QY still
273 presents the most likely seasonal characteristic at most of the heights, with the highest mean
274 values in summer at 1000-2000 m (80.65% in July) and lowest values at 7000-10000 m in late
275 autumn (20.50% in November) in Fig. 6e-f. The elevated RH observed in QY's summer may
276 be related to the sufficient water vapor and large transport volume as QY is located in coastal
277 areas. So the characteristic of QY would be more dependent on water vapor.

278 For comparison, HHHT and YB are relatively random. Over 3000 m in HHHT (Fig. 6a-b), RH
279 in August shows predominantly high values with the highest value of 65.37% at 5000-7000 m.
280 Different from HHHT and QY, the RH profiles in November of YB interestingly show the
281 highest values (83.95%) in the lower atmosphere (0-1000 m) in Fig. 6c-d. It suggests the
282 reduced temperatures observed in autumn of YB promote proximity to saturation conditions,
283 resulting in elevated RH values in November. It is also worth noting that RH above 3000 m in
284 November of YB decreases dramatically as height increases, with the minimum RH of 13.91%
285 at 7000-10000 m. That could be explained by more rapid fluctuations in the water vapor
286 density and temperature in YB in the higher layer under the control of the subtropical monsoon
287 climate zone. Anyway, this plot illustrates a clear decrease in the RH values with heights at
288 three sites.

289 Though there is no obvious RH uncertainty caused by regional differences, we found that QY
290 exhibits the predominant seasonal feature throughout most heights. In contrast, no discernible
291 seasonal characteristics in RH profiles are observed in HHHT or YB. Thus we believe diverse
292 atmospheric circulation patterns and geographical environments could result in regional
293 variations in RH values.

294 *4.3 Case analysis*

295 We selected two different severe convective events in YB (one hailfall and one heavy
296 precipitation) for comparison in Fig. 7. At 23:00 LST on April 15, a thunderstorm with strong
297 winds and hail occurred. The synergetic algorithm retrieved RH profile showed that before
298 22:00 LST, the RH was high (around 90%) at 3000 m height, low (20%-50%) between 3500 m
299 and 8000 m, and above 80% between 8000 m and 9000 m (Fig. 7a). This indicates that before
300 the severe convection, the upper and lower layers were relatively moist, while the middle layer
301 (3500 m-8000 m) was relatively dry (red arrow in Fig. 7a). Such a condition favors the
302 evaporation and cooling of ice particles descending from the upper atmosphere, leading to
303 refreezing and hail formation.

304 In contrast, the RH profile from 25 May to 26 May showed that the entire troposphere
305 (0-10000 m) presented high RH values (>70%) starting at 19:00 LST, which was conducive to
306 heavy precipitation (Fig. 7b). According to ground station observations, YB recorded an hourly
307 rainfall of 52 mm at 21:00 LST, along with gale-force winds of 23 m/s (9th grade). Most areas
308 in YB experienced precipitation, with localized heavy rainstorms. From the above two cases,
309 we can see that the RH in the middle troposphere can be used to distinguish between hail and
310 heavy precipitation during severe convective events.

5. Conclusion

312 This study presents relative humidity (RH) measurements with a developed synergetic
313 algorithm with the combination of Raman lidar, MWR, and satellite at three sites (northern
314 China, middle of China and southern China) from 1 July to 31 November. The methodology
315 for obtaining RH from the synergetic algorithm was introduced. The five-month field
316 campaign was performed and linear regression between the lidar, MWR, satellite, synergetic
317 algorithm and radiosonde data at the range 0-10000 m was presented to testify the accuracy.

318 Strong correlations of RH values over 0.9 were observed between radiosonde measurements
319 and profiles derived from the synergetic approach at three representative sites in China. The
320 lowest MB values (4.93% in HHHT, 2.63% in YB and 2.40% in QY)are observed when lidar
321 data is integrated into the synergetic algorithm, which highlights the accuracy of the lidar data
322 below 3000 m. However, the MB from lidar increased drastically above this height, which
323 suggests the greater applicability of satellite or MWR in the middle and higher layers. In terms
324 of the seasonal characteristic, QY exhibits the predominant seasonal feature throughout most
325 heights, with peak mean values of 80.65% in July at 1000-2000 m and minimal values of
326 20.50% in November at 7000-10000 m.

删除: From 19 to 20 August 2024, due to the continuous southwest warm and humid airflow around the periphery of the subtropical high and the frequent southward weak cold air from the north, large-scale heavy precipitation weather has occurred in Inner Mongolia, Northern, and Central China, …

删除: V

删除: A

删除: V

删除: MVR

删除: Thus, the new synergetic algorithm integrated the best-performing data from various sources with the correction coefficient, which is updated in real-time based on the latest radiosonde data. And that leads to the strong regional applicability of the algorithm.

These results validate the capabilities of the newly developed method to deliver accurate measurements of RH information throughout the troposphere. It also explores the potential of satellite data integration for RH profile retrieval for the first time. However, there are still problems with individual data at certain times during the fusing process. For example, there are few effective data filtered by quality control methods for FY4B data. Therefore, the matching accuracy and more high-quality FY4B data will be improved in future development.

Declaration of Competing Interest

The authors declare that they have no known competing financial interests or personal relationships that could have appeared to influence the work reported in this paper.

Data availability

Raman lidar, MWR, satellite, radiosonde and other auxiliary data used to generate the results of this paper are available from the authors upon request (email: zychen@btbu.edu.cn).

Acknowledgments

This work was supported by the Innovation and Development Special Project of China Meteorological Administration (No. CXFZ2024J011 and CXFZ2024J057) and National Key Research and Development Program of China (No. 2024YFC3711701) . The authors thank the colleagues who participated in the operation of the lidar system at our site. We also acknowledge the CMA for the satellite (FY4B) data, radiosonde data (https://ladsweb.modaps.eosd is.nasa.gov), and the European Center for Medium‐Range Weather Forecasts (ECMWF) for the ERA5 reanalysis data (https://climate.copernicus.eu /climate‐reanalysis).

References

Adam, M., Demoz, B.B., Whiteman, D. N., Venable, D.D., Joseph, E., Gambacorta, A., Wei, J., Shephard, M.W., Milosevich, L. M., Barnet, C. D., Herman, R. L., Fitzgibbon, J., and Connell, R.: Water Vapor Measurements by Howard University Raman lidar during the WAVES 2006 Campaign, J. Atmos. Ocean. Tech., 27, 42-60, https://doi.org/10.1175/2009JTECHA1331.1, 2010.

Bai, W., Zhang, P., Liu, H., Zhang, W., Qi, C., Ma, G., and Li, G.: A fast piecewise-defined neural network method to retrieve temperature and humidity profile for the vertical atmospheric sounding system of FengYun-3E satellite. IEEE Trans. Geosci. Remote Sens. 2023, 61, 4100910.

Barrera-Verdejo, M., Crewell, S., Löhnert, U., Orlandi, E., and Di Girolamo, P.: Ground-based lidar and microwave radiometry synergy for high vertical resolution absolute humidity

删除: No discernible seasonal characteristic in RH profiles are observed in HHHT or YB. Nonetheless, QY exhibits the predominant seasonal feature throughout most heights, with peak mean values of 80.65% in July at 1000-2000 m and minimal values of 20.50% in November at 7000-10000 m. Diverse atmospheric circulation patterns and geographical environments have resulted in regional variations in RH monthly mean values.

删除: V

361   profiling, Atmos. Meas. Tech., 9, 4013-4028, https://doi.org/10.5194/amt-9-4013-2016,
362   2016.

363 Blumberg, W.G., Turner, D.D., Löhnert, U., and Castleberry,S.: Ground based temperature and
364   humidity profiling using spectral infrared and microwave observations, Part II: Actual
365   retrieval performance in clear-sky and cloudy conditions, J. Appl. Meteorol., 54,
366   2305-2319, 2015.

367 Brocard, E., Jeannet, P., Begert, M., Levrat, G. Philipona, R., Romanens, G. and Scherrer, S.C.:
368   Upper air temperature trends above Switzerland 1959-2011, J. Geophys. Res. Atmos., 118,
369   4303-4317, doi:10.1002/jgrd.50438, 2013.

370 Brogniez H., Kirstetter P. E., and Eymard L., Expected improvements in the atmospheric
371   humidity profile retrieval using the Megha-Tropiques microwave payload, Quarterly
372   Journal of the Royal Meteorological Society. 139(673), 842-851,
373   doi.org/10.1002/qj.1869, 2-s2.0-84879241188, 2013.

374 Chen, Z.Y., Ji, C. L., Mao, J. J., Wang, Z. C., Jiao, Z. M., Gao, L. N., Xiang, Y. and Zhang, T.
375   S.: Downdraft influences on the differences of PM2.5 concentration: insights from a mega
376   haze evolution in the winter of northern China, Environ. Res. Lett.,19, 014042, 2024.

377 Cimini, D., Hewison, T., Martin, L., Güldner, J., Gaffard, C., and Marzano, F.: Temperature
378   and humidity profile retrievals from ground-based microwave radiometers during
379   TUC., Meteor. Z., 15, 45-56, https://doi.org/10.1127/0941-2948/2006/0099, 2006.

380 Crewell and U. Lohnert: Accuracy of boundary layer temperature profiles retrieved with
381   multifrequency multiangle microwave radiometry, IEEE T. Geosic. Remote, 45,7,
382   2195-2201, doi: 10.1109/TGRS.2006.888434, 2007.

383 Delanoë, J., and Hogan R. J.: A variational scheme for retrieving ice cloud properties from
384   combined radar, lidar, and infrared radiometer., J. Geophys. Res., 113 (D7): D07204, doi:
385   10.1029/2007JD009000, 2008.

386 Fan, J. Zhang, R., Li, G., Tao, W.K., and Li, X.: Effects of aerosols and relative humidity on
387   cumulus clouds, J. Geophys. Res., 112, D14204, https://doi.org/10.1029/2006JD008136,
388   2007.

389 Foth, A., Baars, H., Di Girolamo, P., and Pospichal, B.: Water vapor profiles from Raman lidar
390   automatically calibrated by microwave radiometer data during HOPE, Atmos. Chem.
391   Phys., 15, 7753-7763, https://doi.org/10.5194/acp-15-7753-2015, 2015.

392 Foth, A. and Pospichal, B.: Optimal estimation of water vapour profiles using a combination of
393   Raman lidar and microwave radiometer, Atmos. Meas. Tech., 10, 3325-3344,
394   https://doi.org/10.5194/amt-10-3325-2017, 2017.

删除: doi:

395 Furumoto, J., Kurimoto, K. and Tsuda, T.: Continuous observations of humidity profiles with
396   the Mu Radar-RASS combined with GPS and radiosonde measurements., J. Atmos.
397   Oceanic. Technol., 20, 23-41, 2003.

398 Gangwar, R. K., Gohil, B. S., Mathur, A. K., Retrieval of Layer Averaged Relative Humidity
399   Profiles from MHS Observations over Tropical Region, J. Atmos. Sci., 645970
400   (10), doi.org/10.1155/2014/645970, 2014.

401 Gohil B. S., Gairola R. M., Mathur A. K., Varma A. K., Mahesh C., Gangwar R. K., and Pal P.
402   K., Algorithms for retrieving geophysical parameters from the MADRAS and SAPHIR
403   sensors of the Megha-Tropiques satellite: Indian scenario, Q. J. Roy. Meteor. Soc. 139
404   (673), 954-963, doi.org/10.1002/qj.2041, 2-s2.0-84879226042, 2013.

405 Granados-Muñoz, M. J., Navas-Guzmán, F., Bravo-Aranda, J. A., Guerrero-Rascado, J.L.,
406   Lyamani, H., Valenzuela, A., Titos, G., Fernández-Gálvez, J., and Alados-Arboledas, L.:
407   Hygroscopic growth of atmospheric aerosol particles based on active remote sensing and
408   radiosounding measurements: selected cases in southeastern Spain, Atmos. Meas. Tech., 8,
409   705-718, https://doi.org/10.5194/amt-8-705-2015, 2015.

410 Hogg, D., Decker, M., Guiraud, F., Earnshaw, K., Merritt, D., Moran, K., Sweezy, W., Strauch,
411   R., Westwater, E., and Little, G.: An automatic profiler of the temperature, wind and
412   humidity in the troposphere, J. Appl. Meteorol., 22, 807-831, 1983.

413 Long, L., He, L., Li, J. B., Zhang, W. L. and Zhang, Y.X.: Climatic characteristics of
414   mesoscale convective systems in the warm season in North China. Meteorol. Atmos,
415   Phys., 135, 21, https://doi.org/10.1007/s00703-023-00958-1, 2023.

416 Kang, Y.Z., Peng, X.D., Wang, S.G., Hu,Y.L., Shang, K.Z.,and Lu, S.: Observational analyses
417   of topographic effects on convective systems in an extreme rainfall event in Northern
418   China, Atmos., Res., 229,127-144,2019.

419 Madonna, F., Amodeo, A., Boselli, A., Cornacchia, C., Cuomo, V., D'Amico, G., Giunta, A.,
420   Mona, L.,and Pappalardo, G.: CIAO: the CNR-IMAA advanced observatory for
421   atmospheric research, Atmos. Meas. Tech., 4, 1191-1208, doi:10.5194/amt- 4-1191-2011,
422   2011.

423 Mattis, I., Ansmann, A., Althausen, D., Jaenisch,V.,Wandinger, U., Müller, D., Arshinov, Y.F.,
424   Bobrovnikov, S.M., and Serikov, I.B.: Relative-humidity profiling in the troposphere with
425   a Raman lidar., Appl. Opt., 41, 6451-6462, doi:10.1364/AO.41.006451, 2002.

426 Mochida, M.: Simultaneous measurements of hygroscopic property and cloud condensation
427   nucleus activity of aerosol particles of marine biogenic origin, Western Pacific Air-Sea
428   Interaction Study, 71-81, America, American Geophysical Union,
429   https://doi.org/10.5047/w-pass.a01.008, 2014.

删除:

Navas-Guzmán, F., Fernández-Gálvez, J. Granados-Muñoz, M.J., Guerrero-Rascado, J. L., Bravo-Aranda,J. A., and Alados-Arboledas, L.: Tropospheric water vapour and relative humidity profiles from lidar and microwave radiometry,Atmos. Meas. Tech., 7, 1201-1211, 2014.

Petters, M.D. and Kreidenweis, S.M.: A single parameter representation of hygroscopic growth and cloud condensation nucleus activity, Atmos. Chem. Phys., 7, 1961-1971, https://doi.org/10.5194/acp-7-1961-2007, 2007.

Ramírez- Beltrán, N. D., Salazar, C. M., Castro Sánchez, J. M., and González, J. E.: A satellite algorithm for estimating relative humidity, based on GOES and MODIS satellite data. Int. J. Remote Sens., 40(24), 9237–9259. https://doi.org/10.1080/01431161.2019.1629715, 2019.

Reichardt, J., Wandinger,U., Klein, V., Mattis,I., Hilber, B., and Begbie, R.: RAMSES: German meteorological service autonomous Raman lidar for water vapor, temperature, aerosol, and cloud measurements, Appl. Opt. 51, 8111-8131, https://doi.org/10.1364/AO.51.008111, 2012.

Schmetz, J.: Good things need time: Progress with the first hyperspectral sounder in geostationary orbit, Geophys. Res. Lett.,48, e2021GL096207, 2021.

Stankov, B.B., Martner, B.E., and Politovich, M.K.: Moisture profiling of the cloudy winter atmosphere using combined remote sensors, J. Atmos. Ocean. Technol., 12 , 488-510, 1995.

Skou, N., Søbjærg, S.S. and Kristensen, S.S.: Future high-performance spaceborne microwave radiometer systems, IEEE Geoscience and Remote Sensing Letters, 19, 1-5, doi: 10.1109/LGRS.2021.3118082, 2022.

Wang, S.F., Lu, F., and Feng.Y.T.: An Investigation of the Fengyun-4A/B GIIRS performance on temperature and humidity retrievals., Atmos. ,13, 1830, 2022.

Toporov, M., and U. Löhnert: Synergy of satellite- and ground-based observations for continuous monitoring of atmospheric stability, liquid water path, and integrated water vapor: theoretical evaluations using reanalysis and neural networks, J. Appl. Meteor. Climatol., 59, 1153-1170, https://doi.org/10.1175/JAMC-D-19-0169.1, 2020

Turner, D.D. and Löhnert, U.: Ground-based temperature and humidity profiling: combining active and passive remote sensors, Atmos. Meas. Tech., 14, 3033-3048, https://doi.org/10.5194/amt-14-3033-2021, 2021.

Wex, H., Stratmann, F., Hennig,T., Hartmann,S., Niedermeier, D., Nilsson, E., Ocskay, R., Rose, D., Salma, I., and Ziese, M.: Connecting hygroscopic growth at high humidities to cloud activation for different particle types, Environ. Res. Lett., 3, 035004, 1-10, 2008.

删除:
Petters, M.D. and Kreidenweis, S.M.: A single parameter representation of hygroscopic growth and cloud condensation nucleus activity, Atmos. Chem. Phys., 7, 1961-1971, https://doi.org/10.5194/acp-7-1961-2007, 2007.

Ware, R., Carpenter, R., Guldner, J., Liljegren, J., Nehrkorn, T., Solheim, F., and Vandenberghe, F.A.: Multi-channel radiometric profiles of temperature, humidity and cloud liquid, radio Sci., 38, 8079-8032, 2003.

Wang, X., Miao, H., Liu, Y., Bao, Q., He, B., Li, J., and Zhao, Y.: The use of satellite data-based 'critical relative humidity' in cloud parameterization and its role in modulating cloud feedback. J. Adv. Model. Earth Sy., 14, e2022MS003213. https://doi.org/10.1029/2022MS003213, 2022.

Wang, Z.Z., Wang, W.Y., Tong, X.L., Zhang, Z., Liu, J.Y., Lu, H.H., Ding, J., Wu,Y.T.: Progress in spaceborne passive microwave remote sensing technology and its application (in Chinese)., Chin. J. Space. Sci., 43(6): 986-1015, doi: 10.11728/cjss2023.06.yg15, 2023.

Whiteman, D.N., Melfi, S.H., and Ferrare, R.A.: Raman lidar system for the measurement of water vapor and aerosols in the earth's atmosphere, Appl. Optics, 31, 3068-3082, https://doi.org/10.1364/AO.31.003068, 1992.

Xu, G. R., B. K., Zhang, W.G., Cui, C.G., Dong, X.Q., Liu, Y.Y. and Yan, G.P.: Comparison of atmospheric profiles between microwave radiometer retrievals and radiosonde soundings., J. Geophys. Res. Atmos., 120, 10, 313-10,323, https://doi.org/10.1002/2015JD023438, 2015.

Yang, J., Zhang, Z., Wei, C., Lu, F., and Guo, Q.: Introducing the new generation of Chinese geostationary weather satellites, Fengyun-4. Bull., Am. Meteorol. Soc. 98, 1637-1658, 2017.

Yang, W., Chen, Y., Bai, W., Sun, X., Zheng, H., and Qin, L.: Evaluation of temperature and humidity profiles retrieved from Fengyun-4B and implications for typhoon assimilation and forecasting, Remote Sens. 15, 5339. https://doi.org/10.3390/rs15225339, 2023.

Yang, J. B., Chen, K., Xu, G. R., Gui, L. Q., Lang, L., Zhang, M.Y., Jin, F., Zhang, R. M., and Sun, C.Y.: Research on neural network training retrieval based on microwave radiometer observed brightness temperature data set, Torrential Rain Disaster (in Chinese), 41, 477-487, https://doi.org/10.3969/j.issn.1004-9045.2022.04.012, 2022.

Zhang, L., Liu, M., He, W., Xia, X.G.,Yu, H.N., Li, S., X., and Li, J.: Ground passive microwave remote sensing of atmospheric profiles using WRF simulations and machine learning techniques., J. Meteorol. Res. 38, 680-692 https://doi.org/10.1007/s13351-024-4004-2, 2024.

Zhang, Z., Dong, X. and Zhu, D.: Optimal channel selection of spaceborne microwave radiometer for surface pressure retrieval over Oceans., J. Atmos. Oceanic Technol., 39, 1857-1868, https://doi.org/10.1175/JTECH-D-21-0121.1, 2022.

Zieger, P., Fierz-Schmidhauser, R., Weingartner, E., and Baltensperger, U.: Effects of relative humidity on aerosol light scattering: results from different European sites, Atmos. Chem. Phys., 13, 10609-10631, https://doi.org/10.5194/acp-13-10609- 2013, 2013.

List of Tables

Table 1 Instruments and monitoring parameters

Instrument	Parameters/units	Temporal-spatial Resolution
Raman lidar	Relative humidity (RH)	7.5 m, 3 minutes
Microwave radiometer (MWR)	Temperature (^{O}C), Relative humidity (RH)	50 m, 3 minutes
FY4B	Relative humidity (RH)	1 hour

Table 2 Assessment of the accuracy of four RH retrieval results (lidar, MWR, satellite and synergetic algorithm) compared with radiosonde at 47 sites in China.

Comparison with radiosonde	Number of sample	R	MB (%)	MAB (%)	RMSE (%)
lidar	192111	0.91	0.56	6.7	10.67
MWR	192111	0.82	-1.49	10.79	14.31
satellite	192111	0.74	1.08	13.19	17.02
syngenetic algorithm	192111	0.98	0.42	3.24	5.27

Table 3 The same as Table 2 but at three representative sites in China.

	Comparison with radiosonde	Number of sample	R	RMSE (%)
HHHT (northern China)	lidar	3771	0.83	20
	MWR	3771	0.74	25
	satellite	3771	0.76	24
	syngenetic algorithm	3771	0.94	10
YB (middle China)	lidar	7542	0.86	19
	MWR	7542	0.80	26
	satellite	7542	0.83	29
	synergetic algorithm	7542	0.92	12
QY (southern China)	lidar	8110	0.86	18
	MWR	8110	0.75	19
	satellite	8110	0.66	21
	synergetic algorithm	8110	0.93	11

删除: HHHT
(northern China)
Comparison with radiosonde
Number of sample
R

516
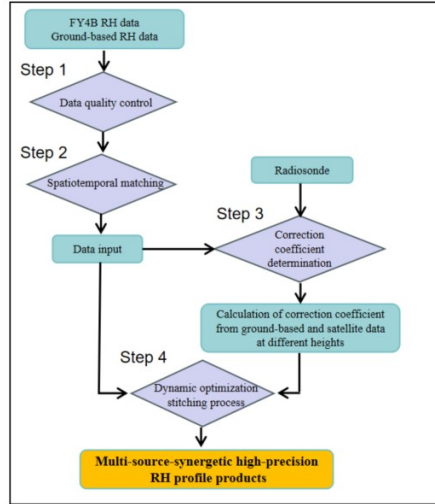
517 **Fig. 1** Sketch of the retrieval scheme. Details are given in the text.

518

519

520

521
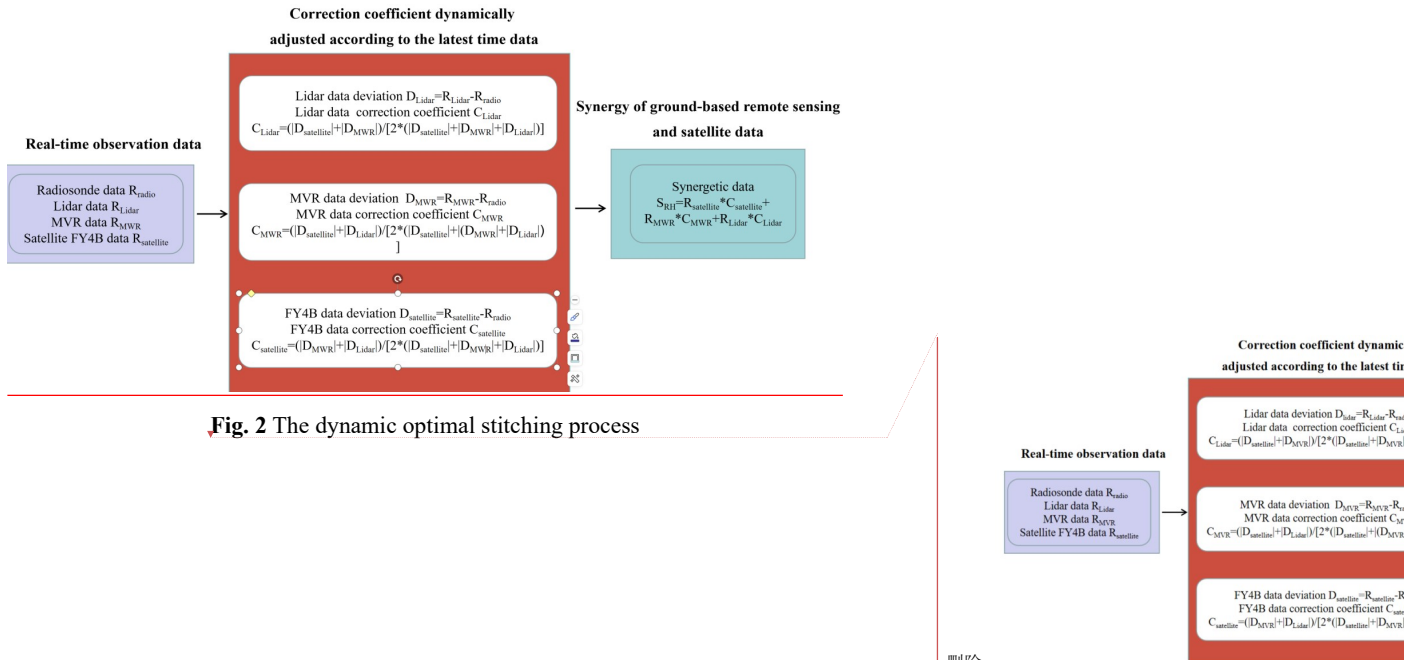
522 **Fig. 2** The dynamic optimal stitching process

523

删除:
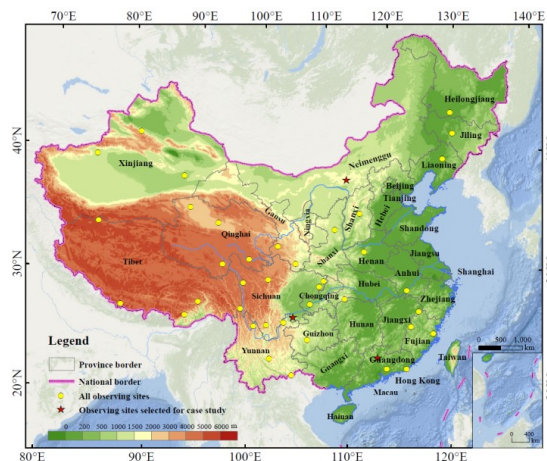
Fig. 3 The observing sites (yellow circles) and three selected sites (red stars) for statistics and case studies are marked in the
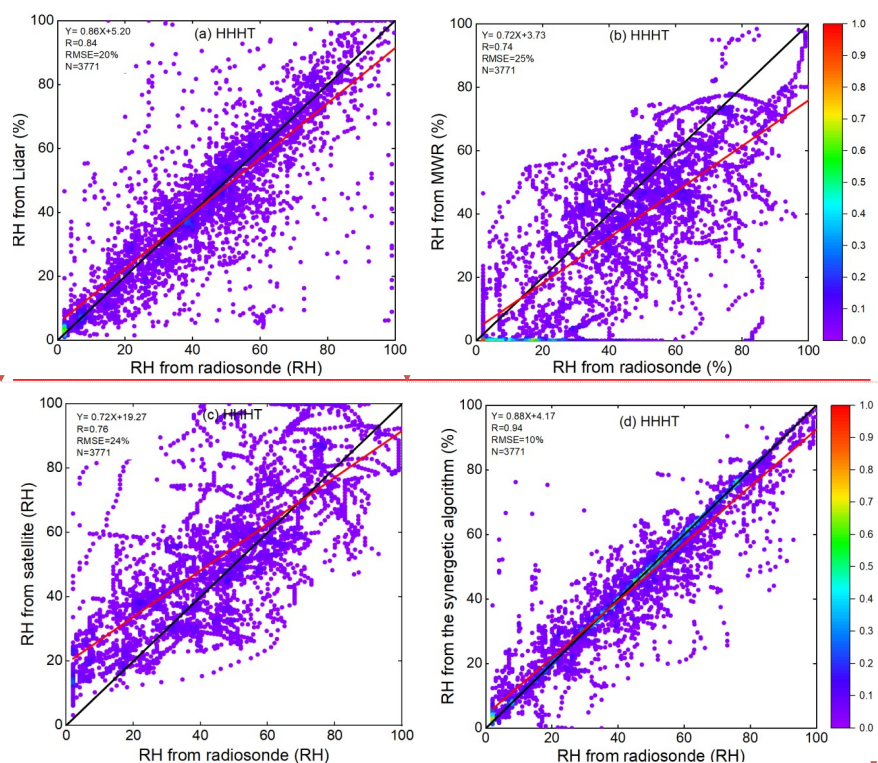
删除： map.

删除：

删除：

删除：

删除：

删除：

531

532

533

534
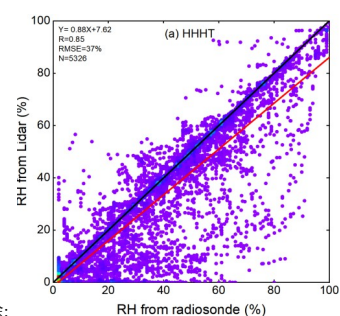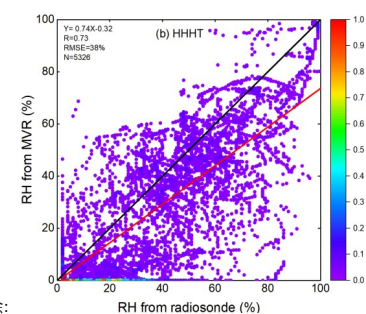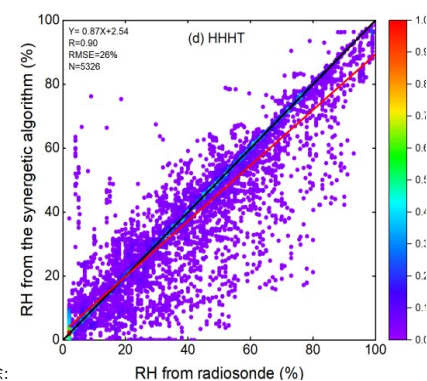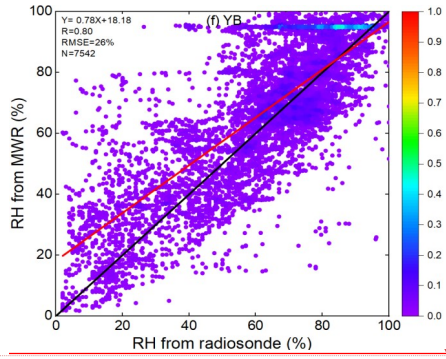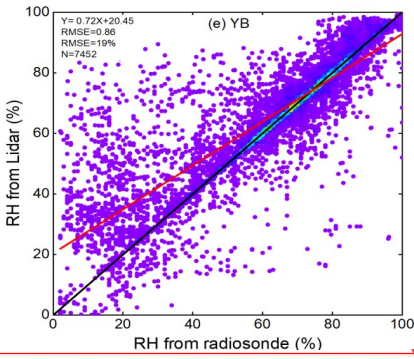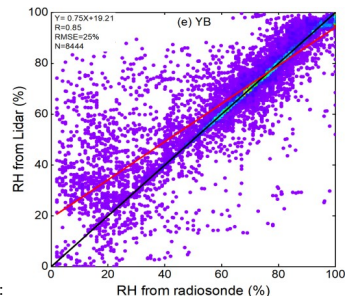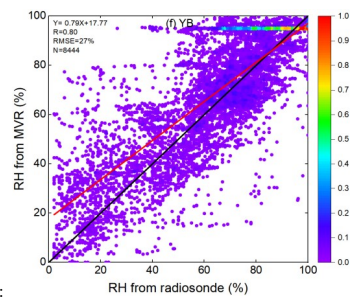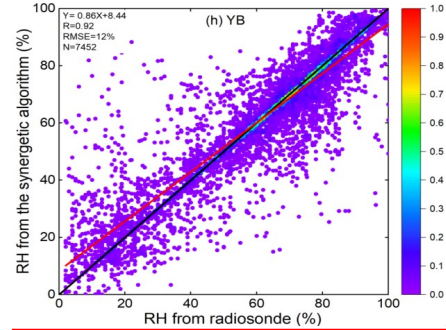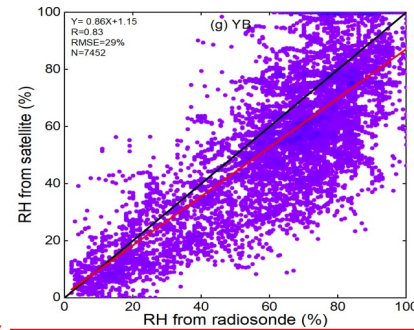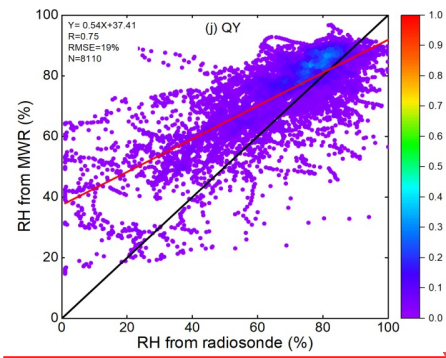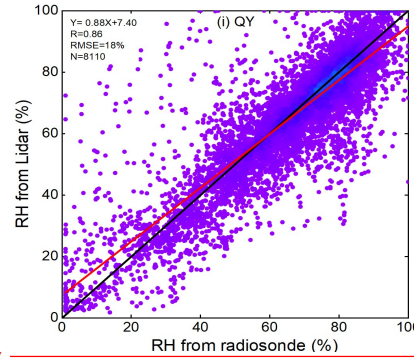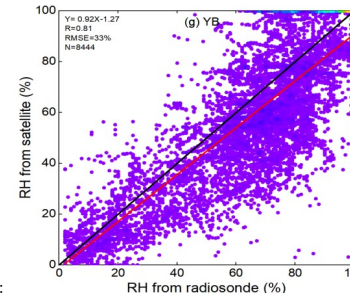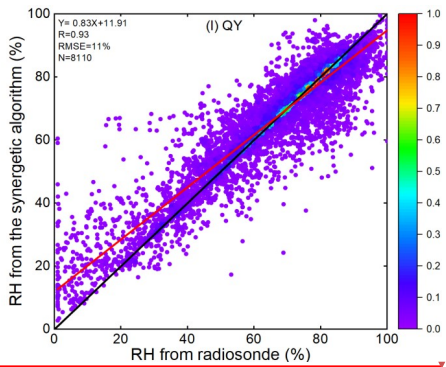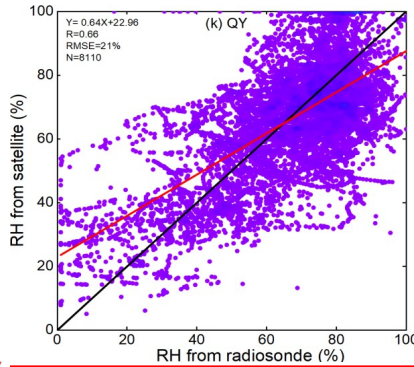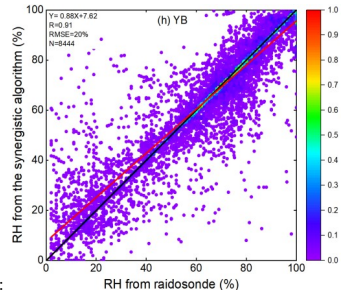
删除:
删除:
删除:
删除:
删除:
删除:
删除:
删除:
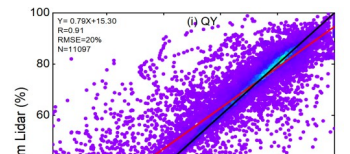
535 **Fig. 4** Four-methods-retrieved RH results (lidar, MWR, satellite and synergetic algorithm)
536 compared with radiosonde at three sites in China from 1 July to 31 November 2024. (a)
537 Comparison between lidar and radiosonde in HHHT, (b) Comparison between MWR and
538 radiosonde in HHHT, (c) Comparison between satellite and radiosonde HHHT, (d)
539 Comparison between synergetic algorithm and radiosonde in HHHT; (e)-(h), the same as (a)-(d)
540 but in YB. (i)-(l), the same as (a)-(d) but in QY. The red line shows the regression line. The
541 black line is the one-to-one line.

542

543

544
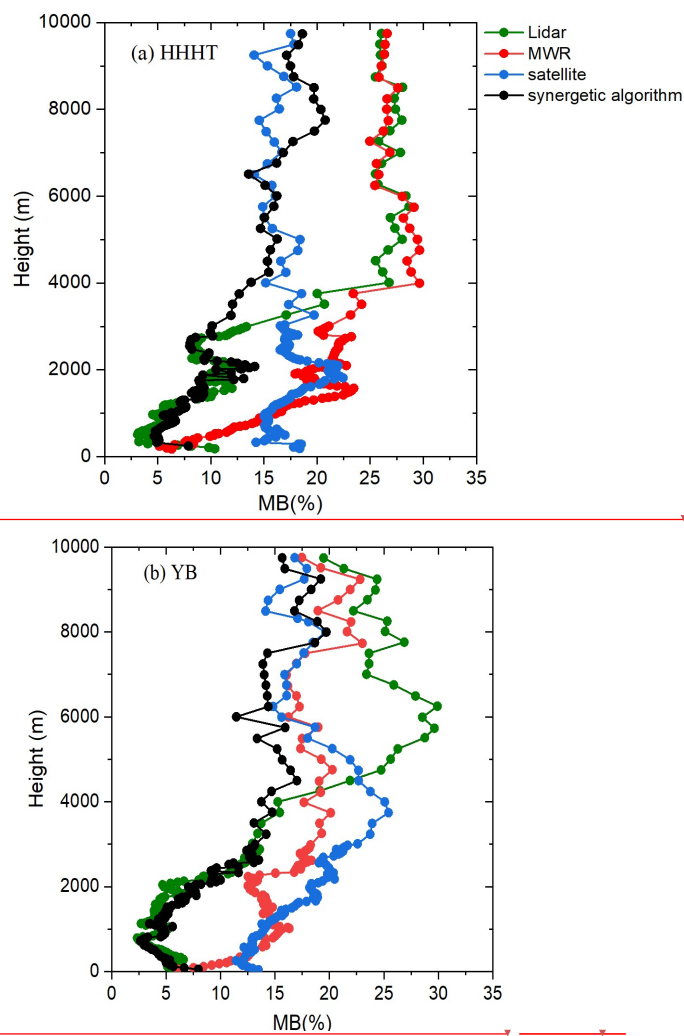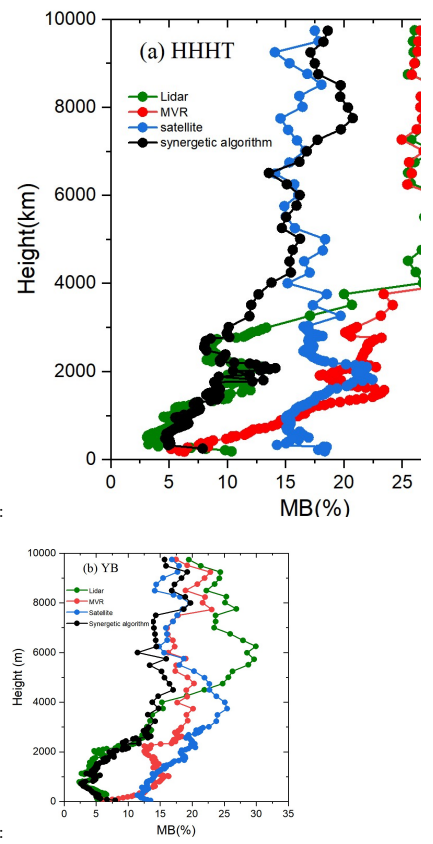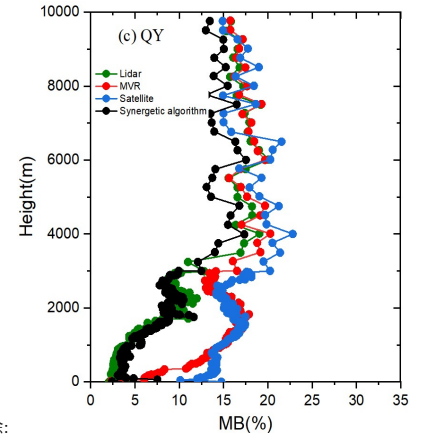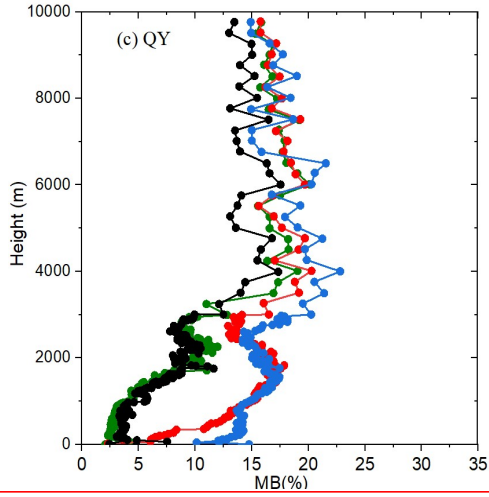
Fig. 5 RH vertical mean bias (MB) profiles retrieved from lidar, MWR, satellite and synergetic algorithm compared to the radiosonde data in (a) HHHT, (b) YB and (c) QY.

551
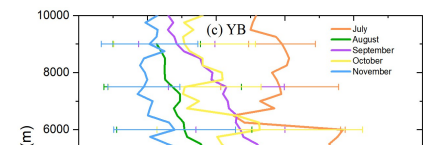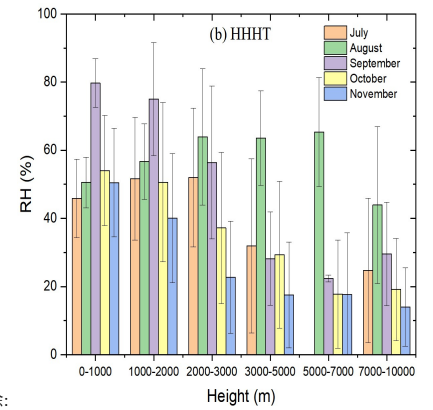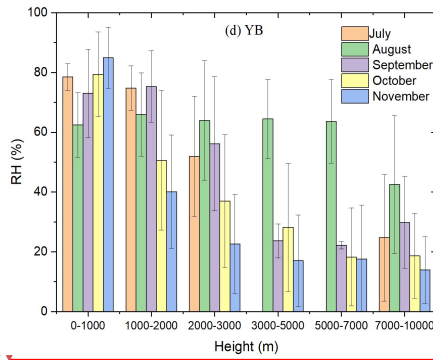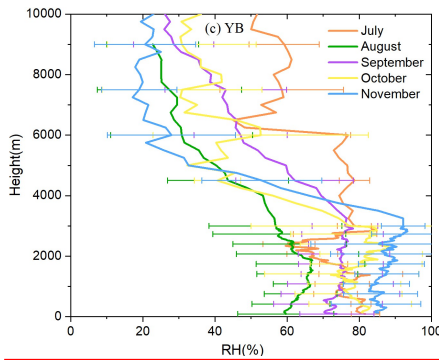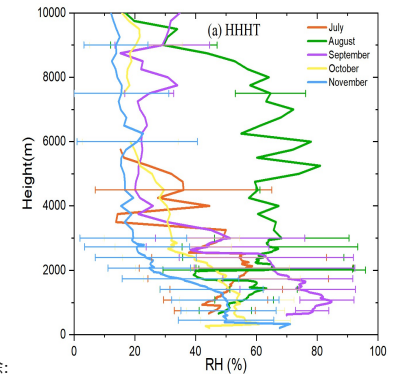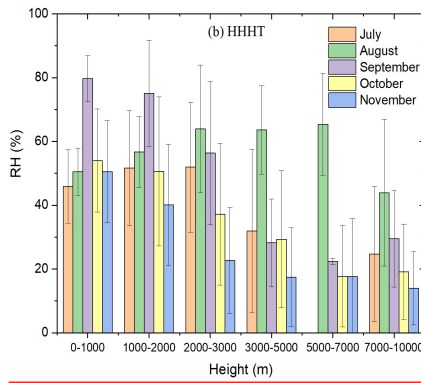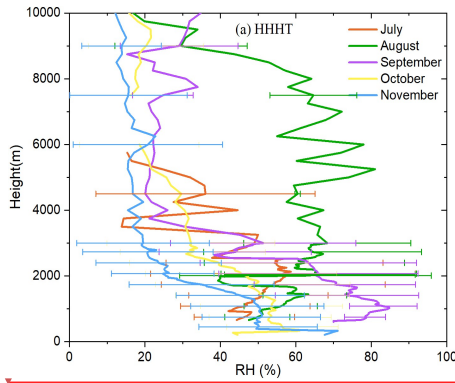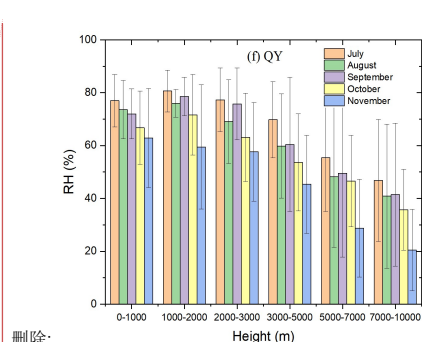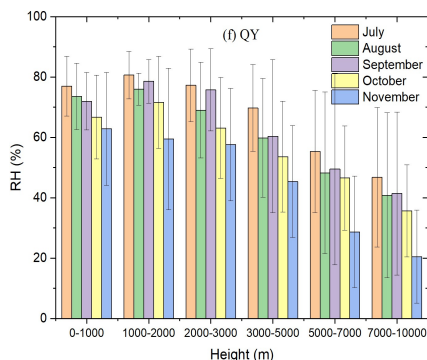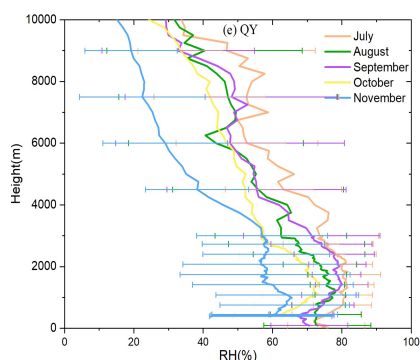
Fig. 6 RH Monthly vertical profiles (left) and monthly mean values for different heights (right)

in (a)-(b) HHHT, (c)-(d)YB and (e)-(f) QY. The error bars indicate the standard deviation.
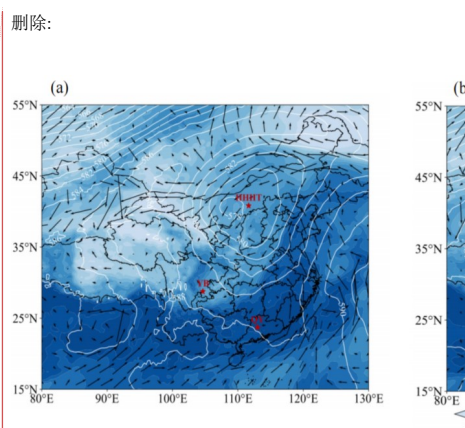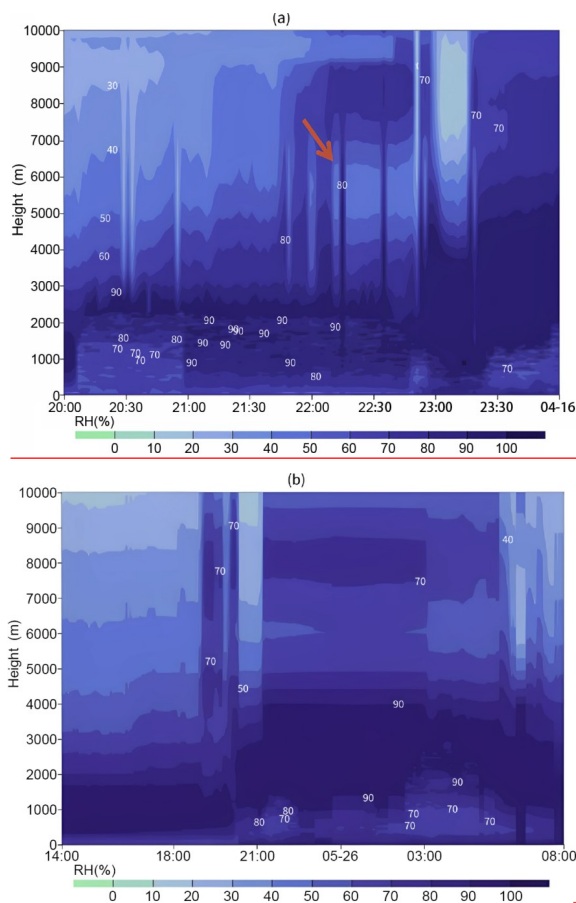
554

557 **Fig. 7** Height-time display of RH from the synergetic retrieval during two convective cases (a)

from 20:00 LST to 23:30 LST 15 April and (b) from 14:00 LST 25 May to 08:00 LST 26 May 2024 in YB. The red arrow indicates the less humidity in the layer when the hailfal occurred in the first convective case.